

## *In Situ* Spectroscopic Study of the Optomechanical Properties of Evaporating Field Ion Emitters

P. Dalapati,<sup>1,†</sup> G. Beainy,<sup>1</sup> E. Di Russo,<sup>1</sup> I. Blum<sup>①</sup>,<sup>1</sup> J. Houard,<sup>1</sup> S. Moldovan,<sup>1</sup> A. Vella,<sup>1</sup> F. Vurpillot,<sup>1</sup> N. Le Biavan,<sup>2</sup> M. Hugues,<sup>2</sup> J.M. Chauveau,<sup>2</sup> and L. Rigutti<sup>①</sup>,<sup>1,\*</sup>

<sup>1</sup>UNIROUEN, CNRS, Groupe de Physique des Matériaux, Normandie Université, 76000 Rouen, France

<sup>2</sup>Université Côte d'Azur, CNRS, CRHEA, 06560 Valbonne, France



(Received 25 September 2020; revised 12 October 2020; accepted 8 January 2021; published 5 February 2021)

The possibility of measuring *in situ operando* photoluminescence spectroscopy within a photonic atom probe allows for the real-time study of the mechanical stress state within a field emitter either statically, as a function of the field-induced tensile stress, or dynamically, as a result of the evolution of the shape of the emitter upon its evaporation. Dynamic evolution results from the relaxation of strain induced by lattice mismatch and by the propagation of stress from the apex, while the morphology of the field emitter changes. Optomechanical information can be interpreted through the three-dimensional atomic scale images of the chemical composition of the emitter obtained through standard atom probe analysis. Here, the photoluminescence signal of a ZnO/(Mg,Zn)O quantum well allows for the local measurement of strain within the well and of the electrostatic field applied to the apex of the nanoscale field emitter.

DOI: [10.1103/PhysRevApplied.15.024014](https://doi.org/10.1103/PhysRevApplied.15.024014)

### I. INTRODUCTION

The measurement of strain states in nanoscale systems is possible nowadays by means of different techniques. Remarkable situations include the measurement of strain in transmission electron microscopes (TEMs) by geometric phase analysis [1] or holographic interferometry [2] in field-effect transistors, heterostructures, and nanowires. Access to the strain state can also be obtained by cross-section scanning tunneling microscopy, generally by measurement of the relief of the scanned surface due to out-of-plane lattice relaxation in semiconductor superlattice or quantum-dot structures [3,4], as well as in metallic structures [5]. Alternatively, three-dimensional (3D) strain-stress maps can be obtained by x-ray nanoprobe from synchrotron light [6,7].

Strain may have an important effect on the optical and electrical properties of nanoscale systems. Strain engineering may be appropriate for the manipulation of energy bands and can influence the optical signature of emitting or absorbing centers [8,9] and electrical transport in semiconducting channels [10]. It may be applied by the proper design of the nanoscale system, for instance exploiting lattice mismatch in heterostructures [9], or by an external

action producing hydrostatic [11,12] or uniaxial stress [13,14] in a controlled way.

Herein, we report on an original way to access to the stress state of nanoscale field ion emitters through the use of a photonic atom probe (PAP) [15,16], the principles of which are schematically illustrated in Fig. 1. This instrument consists of a laser-assisted tomographic atom probe, in which a needle-shaped nanoscale specimen (field ion emitter) is progressively submitted to the evaporation of constituent ions under the combined action of a static dc field and laser pluses, which trigger the process. As in any tomographic atom probe, ion evaporation provides a 3D image of the chemical composition of the specimen. The particular feature of the PAP instrument is that light collection optics is applied to the *in situ* analysis of photoluminescence (PL) produced by the field emitter under the same laser excitation used for ion evaporation. As a result, it is possible to obtain a 3D image of quantum emitters coupled with their optical signature. However, beyond interest in this instrument in the framework of nanoscale microscopy, we demonstrate here that the PAP allows for the *in situ* operando measurement of the strain state of a field emitter, which is due to both strain relaxation as a result of the evaporation of heterostructure layers with different lattice constants and to the application of the dc field responsible for evaporation of the specimen.

This work is structured as follows. Section II describes the experimental techniques and methods. Then, the PAP analysis of ZnO/(Mg,Zn)O quantum-well (QW) heterostructures is presented in Sec. III. In Sec. IV the theory

\*lorenzo.rigutti@univ-rouen.fr

†Present address: Research Center for Nano-Devices and Advanced Materials, Nagoya Institute of Technology, Nagoya 466-8555, Japan.

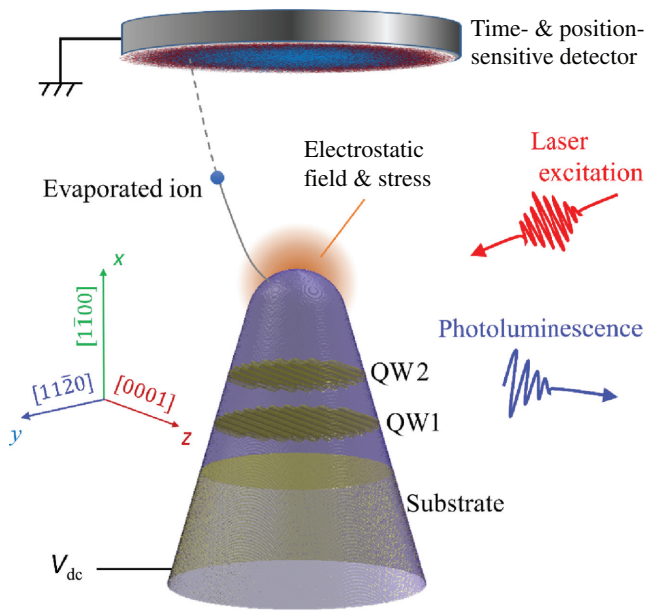


FIG. 1. Schematic representation of the experimental setup and analyzed system. Orientation of the crystal constituting the field emitter is also reported.

of stress and strain in nonevaporating and evaporating field emitters is developed. Finally, the connection between theory and experiment is made in the discussion of Sec. V.

## II. EXPERIMENT

### A. Sample growth and properties

Plasma-assisted molecular beam epitaxy (MBE) is used to grow the ZnO/(Zn,Mg)O homoepitaxial QWs on an  $m$ -plane (1-100) wurtzite (WZ) ZnO substrate. Details on homoepitaxial growth can be found in Ref. [17]. The structures contain two ZnO QWs and (Mg, Zn)O barriers. The total thickness and alloy composition of the multilayer structure are designed to avoid plastic relaxation.

### B. Tip specimen preparation

Needle-shaped field emitters are prepared by using the focused ion beam (FIB) in a ZEISS Nvision40 dual-beam SEM FIB system. The preparation consists of a standard protocol of lift out and milling using an acceleration voltage of 30 kV for Ga ions during sample milling, with a final cleaning step at 2 kV [18]. This protocol is designed to preserve the PL signal from QW1 and from the (Mg, Zn)O barrier detectable in the PAP system, while the signal of QW2 (closer to the tip apex) is generally quenched by damage introduced by the Ga ions. With ions at 30 keV, the FIB is expected to produce surface amorphization over several nanometers at grazing incidence and introduce nonradiative recombination centers over several tens of nanometers [19]. In the present structures, the FIB

induces irreversible damage to the optical properties over the whole region of interest of around 50% of the fabricated tips. In the latter case, only the signal of the ZnO substrate is detectable. Several tip specimens are analyzed in this work, yielding consistent results. Notably, alternative preparation methods could be considered to increase the success rate for the preparation of specimens from thin films, such as using a plasma FIB [20], which is known to introduce less impurities, or directly synthesize quantum-emitter structures within nanowires [21]. The tip specimen for which the detailed analysis is reported herein is visible in the scanning electron micrograph presented in Fig. 2(a).

### C. Tip specimen preliminary characterization and crystal orientation

Transmission electron microscopy (TEM) assays are carried out on prepared tip specimens with a double-corrected analytical JEOL JEM-ARM200CF instrument operated at 200 kV. During scanning TEM (STEM) experiments, a 0.9 Å probe scans the specimen surface and two simultaneous micrographs are registered under a bright-field circular detector and a high-angle annular dark field (HAADF) detector. In HAADF detection, the image intensity approximately scales with the square of the  $Z$  atomic number of the material under examination. The high-intensity areas correspond to regions rich in Zn, allowing one to determine the thickness of the QWs by direct measurements. The thicknesses of the QWs measured by STEM HAADF are  $t_1 = (2.0 \pm 0.1)$  nm and  $t_2 = (3.9 \pm 0.1)$  nm. Notably, as STEM performed at 200 keV may introduce nonradiative recombination centers, the tip specimen reported in Fig. 2(b) is not one of those analyzed by the PAP. The sawtooth profile of the QWs clearly marks the morphology of these QWs. This profile is actually that of the ZnO substrate surface before epitaxial growth of the multi-QW-barrier system, and it propagates throughout the epitaxial growth of the latter [22]. This profile is susceptible to the induction of compositional inhomogeneities within the barriers, with the formation of Zn- and Mg-enriched regions, corresponding to the edges pointing towards the substrate and towards the upper surface, respectively. The results reported in Fig. 2(b) and later in the Sec. III dedicated to the PAP study show that the barriers exhibit a decomposition behavior similar to that reported in the detailed study reported in Ref. [22]. These compositional inhomogeneities are related to the sawtooth morphology. No evidence for the presence or introduction of dislocations or other extended defects is found.

All prepared tips have the axis oriented along the  $[1\bar{1}00]$  direction ( $m$  direction) of the wurtzite crystal, which also corresponds to the  $x$  axis of the reference system in which the stress-strain tensors are defined. The sawtooth profile is visible when the observation is performed along the polar

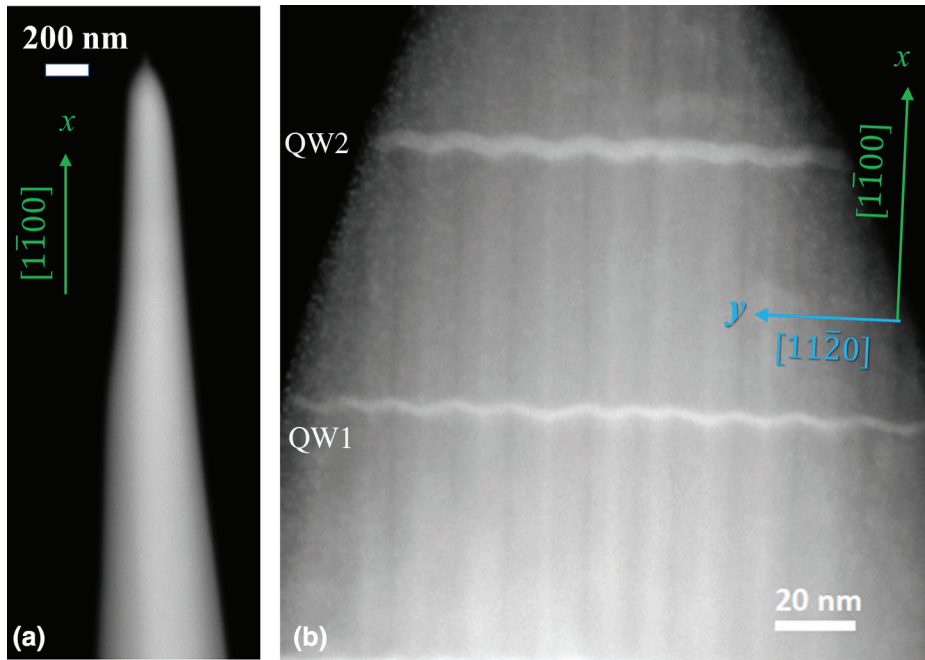


FIG. 2. (a) Scanning electron micrograph of the tip under analysis. (b) Transmission electron micrograph and crystal orientation of a field emitter extracted from the ZnO/(Mg, Zn)O heterostructure system.

[0001] direction ( $c$  direction,  $z$  axis for the strain-stress tensors) [22]. The  $[11\bar{2}0]$   $a$  direction corresponds to the  $y$  axis for the strain-stress tensors. The orientation of the crystal is also visualized in Fig. 1 and the correspondence between the tip reference frame and crystal directions is specified in Table I.

#### D. Photonic atom probe setup

As mentioned in Sec. I, the PAP is illustrated in Fig. 1, while the technical details of the instrument used in this study are discussed in Ref. [15]. The nanometer-scale needle-shaped specimen is polarized with voltage  $V_{dc} = 3\text{--}16$  kV, leading to an apex electric field of a few tens of V/nm [23,24]. Field ion evaporation is then triggered by femtosecond laser pulses at a repetition rate of 400 kHz. The specimen apex is illuminated by a laser spot with a size close to  $1\ \mu\text{m}$  and an average power of  $10\ \mu\text{W}$ . The spot size is limited by imperfections in the optical elements and is larger than the diffraction limit of  $w \approx \lambda/(2\text{NA}) = 443$  nm, where  $\lambda = 266$  nm is the laser wavelength and  $\text{NA} = 0.3$  is the numerical aperture of the focusing optics. PL spectra are acquired with a 600 mm grating in a 320 mm focal-length spectrometer, with a spectral resolution of around 0.3 nm. The CCD array integration time for each acquisition is set to 90 s.

TABLE I. Correspondences between the tip frame and the crystal directions.

Directions in the tip reference frame		Crystal directions	
Tip axis	$x$	$[1\bar{1}00]$	$m$
	$y$	$[11\bar{2}0]$	$a$
	$z$	$[0001]$	$c$

The evaporated ions are detected by a time-resolved and position-sensitive detector [25], which provides the impact position of ions and their time of flight. The first piece of information is used to calculate the position of evaporated atoms at the tip surface, while the second is used to compute mass-to-charge ratios that enable the chemical nature of ions to be identified, as shown in the mass spectrum of Fig. 3(a). The in-depth layer-by-layer evaporation of the specimen makes the 3D reconstruction of atomic positions possible. The 3D maps of the chemical composition of the specimen can thus be derived. The instrument is able to collect and analyze *in situ* and *operando* the photoluminescence that laser pulses excite simultaneously with surface-atom evaporation.

The collection of the PL signal during atom probe tomography (APT) translates into a series of spectra that are indexed by the integer  $i_{\text{PL}}$ , while keeping track of the progressive number of detected atoms. This has recently been shown to enable superresolution optical spectroscopy, as spectral signatures of closely lying emitters can be discriminated. This possibility is not exploited herein, in which a single emitter is studied [16]. PL is also collected during a slow initial voltage ramp, with steps at set bias values, to obtain complementary information on the field-induced strain [26,27].

### III. PHOTONIC ATOM PROBE EXPERIMENT

In the following, the PAP experiment is described. After the initial voltage ramp, evaporation takes place at a detection rate set in the interval of  $\Phi = 0.003\text{--}0.004$  ions/pulse. The specimen base temperature is set at 30 K.

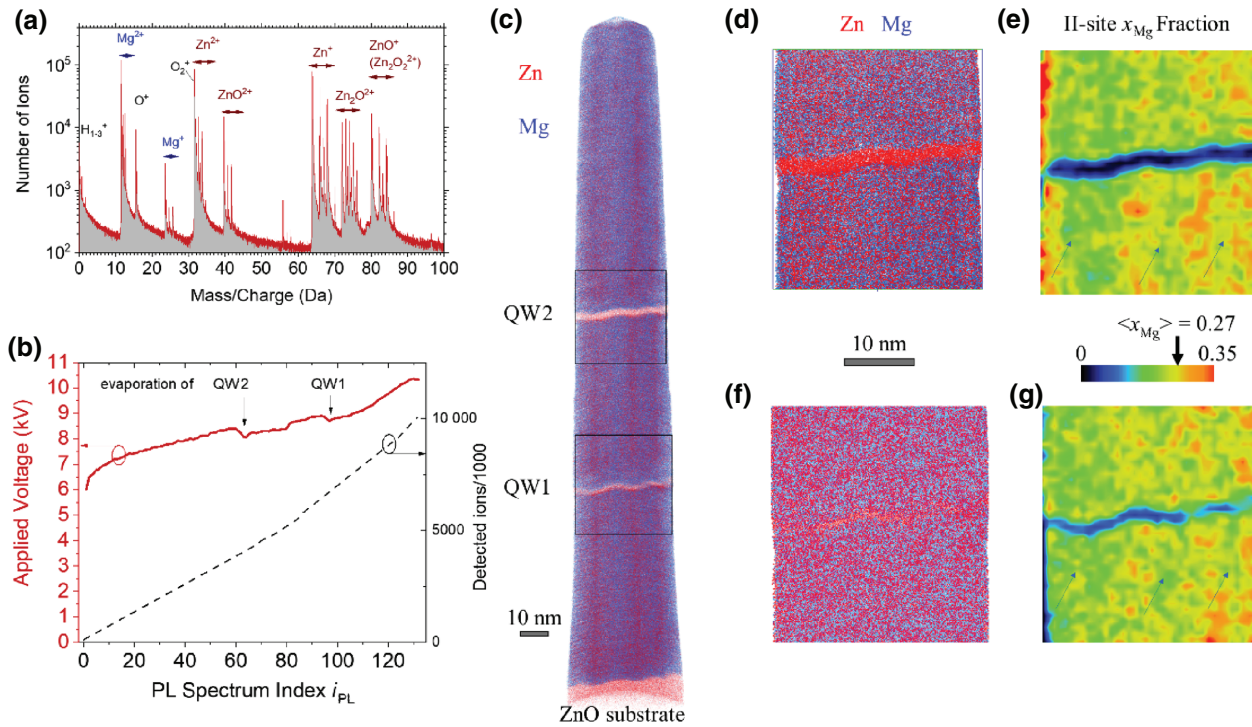


FIG. 3. Atom probe tomography analysis. (a) Mass spectrum indicating the main ionic species. (b) Voltage curve and progressive number of detected atoms as a function of the index of the PL spectrum  $i_{PL}$ . (c) Three-dimensionally reconstructed volume of the analyzed field emitter. All Mg ions are reported in blue; 30% of  $Zn^+$  and  $Zn^{2+}$  ions are reported in red (both classes of detection events are traced with a 0.2 level of transparency). (d) Magnification of the distribution of Zn and Mg ions in a 5-nm-thick slice intersecting the axis of the tip at the depth of QW2, (e) II-site fraction map of the slice reported in (d). (f) Magnification of the distribution of Zn and Mg ions in a 5-nm-thick slice intersecting the axis of the tip at the depth of QW1. (g) Compositional map of the slice reported in (f). Arrow above the color scale indicates the average value of the Mg II-site fraction  $\langle x_{Mg} \rangle = 0.27$  of the (Mg, Zn)O barrier.

### A. Mass spectrum

The mass spectrum is shown in Fig. 3(a), and it contains the atomic and molecular ionic species usually found in the analysis of (Mg, Zn)O [22,28]. The interpretation of mass spectra should consider the superimposition of peaks associated with different atomic and molecular species: the peak at 32 Da corresponds to an overlap of  $^{64}Zn^{2+}$  and  $O_2^+$  [22]. Considering the natural abundance of Zn isotopes in the mass range of 31–37 Da, it is possible to calculate the respective total amount of zinc and oxygen; the same method is adopted in the mass range of 78–89 Da, where the existing peaks are attributed to both  $ZnO^+$  and  $Zn_2O_2^{2+}$ . Analysis of the  $Zn^{2+} - to - Zn^+$  charge-state ratio is a useful indicator of the intensity of the microscopic field (i.e., the field responsible for ion evaporation, which is usually higher than the average field) [29]. This ratio is approximately equal to 0.5 through the barrier, which indicates that the field may be assumed as constant. Furthermore, this ratio corresponds to a microscopic field of  $F_\mu \sim 20$  V/nm, which is favorable for composition measurements in (Mg, Zn)O [28]. Separate APT analysis is performed with another instrument (a laser-assisted

wide-angle tomographic atomic probe, which is used in recent works on composition metrology [28,30]) to confirm measurements of the composition within the barriers.

### B. Voltage curve

The voltage applied to the tip is reported in Fig. 3(b) versus the index,  $i_{PL}$ , of the PL spectra acquired during tip evaporation. The same plot also contains the relationship between the PL spectral index and the number of detected atoms. Evaporation takes place between  $V_{es} = 6$  kV (starting evaporation voltage) and  $V_{ef} = 10.3$  kV (final evaporation voltage). The ratio between these two values is fairly consistent with the ratio of the initial and final radii, which can be visually assessed by the analysis of the SEM image of the tip [Fig. 2(a)], i.e.,  $R_i = (48 \pm 5)$  nm and  $R_f = (88 \pm 5)$  nm. The continuous increase in the radius of the tip during evaporation forces a rise of the voltage to maintain a constant detection rate. Remarkably, the curve is nonmonotonous: two dips are clearly visible after  $i_{PL} = 60$  and 95. These local minima correspond to the evaporation of the two ZnO QWs, which have a lower cohesive energy than that of their surrounding (Mg, Zn)O

barriers, and consequently, the surface field needed for evaporation at a constant detection rate is lower. The local decrease of the applied voltage translates into a decrease of the apex field intensity. The experiment is concluded when evaporation reaches the ZnO substrate.

### C. 3D reconstruction

The 3D reconstructed volume of the analyzed system is visualized in Fig. 3(c), and it is obtained by the application of a reconstruction algorithm based on the evolution of the applied voltage [31]. The following set of parameters is used: apex field = 16.8 V/nm, projection point  $m + 1 = 1.65$ , curvature factor = 1.5, and reconstruction detection efficiency  $\eta_{\text{rec}} = 0.35$ . In Fig. 3(c), 30% of the detected Zn-containing ions (red) and 100% of the detected Mg ions (blue) are shown, both with a transparency of  $\alpha = 0.2$ . These visualization parameters make the main morphological and chemical features of this heterostructure system quite clear. Notably, the exterior boundary of the reconstruction corresponds to an interior region of the tip (corresponding to the field of view of the ion detector), and hence, does not match the entire projected morphology exhibited by the HAADF image presented in Fig. 2(b).

#### 1. Morphological and chemical features of the heterostructure

Both QW1 and QW2 present a serrated profile with the groove edges aligned along the WZ  $c$  axis. Their thicknesses,  $t_1 = (2.0 \pm 0.2)$  nm and  $t_2 = (4.1 \pm 0.3)$  nm, are consistent with the TEM analysis. The morphologies of both are shown in detail in the magnified 5-nm-thick slices intersecting the tip axis in Figs. 3(d) and 3(f). The same orientation of the reconstructed volume illustrates very clearly the decomposition effect within the (Mg, Zn)O barriers already discussed in the Sec. II on preliminary TEM characterization and in previous studies [16,22]. This phenomenon is reproduced through the depth of the analyzed volume in Fig. 3(c) and is also visible in the composition maps realized on the 5-nm-thick slices intersecting the tip axis reported in Figs. 3(e) and 3(g). This effect consists of Zn accumulation ( $x_{\text{Mg}} \sim 0.22$ ) corresponding to the groove-edge  $a$ -type planes pointing towards the substrate, while Mg is at a higher concentration ( $x_{\text{Mg}} \sim 0.35$ ) in the planes corresponding to groove edges pointing towards the epitaxial layer surface. The average composition of the barrier corresponds to the II-site Mg fraction of  $\langle x_{\text{Mg}} \rangle = 0.27$ . Finally, we observe that the substrate-barrier interface, visible at the base of the reconstructed volume of Fig. 3(c), exhibits the groove profile that is transferred to the whole heterostructure morphology during epitaxial growth [22].

### D. PL spectra

#### 1. Spectral components and energy shifts during the initial voltage ramp (constant geometry)

The PL spectra acquired during the voltage ramp, with no evaporation (except for the last step, in which the evaporation flux was very low,  $\Phi \sim 2 \times 10^{-4}$  ion/pulse), are reported in Fig. 4(a). During this ramp, the tip shape does not evolve, but only the applied bias (and the surface field) changes. Three spectral components can be clearly identified within the spectra. The peak at an energy of  $E = 3.34$  eV is related to the ZnO substrate. It is composed of a main peak and by phonon replica at lower energy. It is not possible to exactly localize the emission, as the ZnO section illuminated by the excitation laser is around

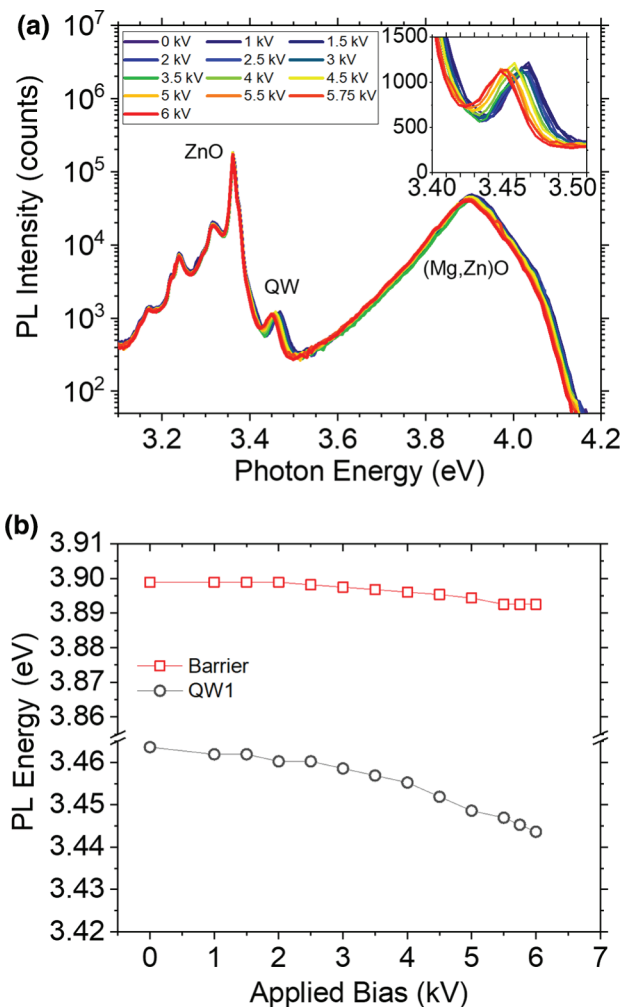


FIG. 4. Photoluminescence of the analyzed field emitter during the initial bias ramp. Tip shape does not change, as no evaporation takes place. (a) PL spectra. Inset is a magnification of the QW1 luminescence. (b) Peak energies of emissions of the (Mg, Zn)O barrier (red squares) and QW1 (black circles) reported as a function of the voltage applied to the tip,  $V_{\text{dc}}$ .

1  $\mu\text{m}$  long. The ZnO peak shifts extremely weakly during the bias ramp. It should be mentioned, however, that peak broadening towards lower energies is found in other tip specimens from the same batch.

The asymmetric peak at  $E_{\text{barr}} = 3.89$  eV in the unbiased tip originates from the (Mg,Zn)O barrier. Its energy is consistent with the measured barrier composition and with previous studies [28,32]. It has a full width at half maximum (FWHM) of  $\Gamma_{\text{barr}} = 0.1$  eV. The (Mg,Zn)O peak slightly redshifts as a function of the applied bias, as shown quantitatively in Fig. 4(b). The peak energy shifts from 3.90 to 3.85 eV during the ramp up to 6 keV. The trend of the energy also indicates parabolic behavior rather than linear behavior. The emission from the (Mg,Zn)O barrier can originate from the whole length of the tip. However, it is more likely that only the (Mg,Zn)O section below QW1 contributes to the optical signal. This assumption is motivated by the fact that the signal of the upper QW2 is not visible, indicating that the optical properties of the field emitter are degraded in its upper part by the action of the FIB during specimen preparation. In any case, (Mg,Zn)O extends to a depth of around 100 nm, which contains a sufficiently large optically active volume.

The signal of QW1 is found at  $E_{\text{QW1}} = 3.462$  eV in the unbiased tip. It is weak with respect to the other two

peaks, but it is well defined even if it is superimposed on the high-energy tail of the ZnO peak. The inset in Fig. 4(a) underlines the details of the peak redshift when  $V_{\text{dc}}$  increases. The evolution of the peak energy is reported in Fig. 4(b) as a function of the bias. Similarly to the case of the (Mg,Zn)O peak, the QW1 peak gradually shifts from 3.462 to 3.443 eV. The FWHM remains close to the unbiased value,  $\Gamma_{\text{QW1}} = 20$  meV. What is crucial about the QW1 signal is that its emission can be very precisely localized within 2 nm of its layer thickness. This makes QW1 a local optical probe for the environmental parameters that can influence its optical signature during the experiment.

All peak intensities remain constant throughout the initial bias ramp.

## 2. Energy shifts during evaporation (quasiconstant field)

The evolution of the PL spectra during specimen evaporation and the relationship between the PL spectrum index,  $i_{\text{PL}}$ , and the reconstructed APT volume are shown in Figs. 5(a) and 5(b), while Fig. 5(c) is a magnification of the QW1 spectral region. The series of PL spectra shown here as a two-dimensional (2D) color plot, which better allows the energy trends during the experiment to be followed.

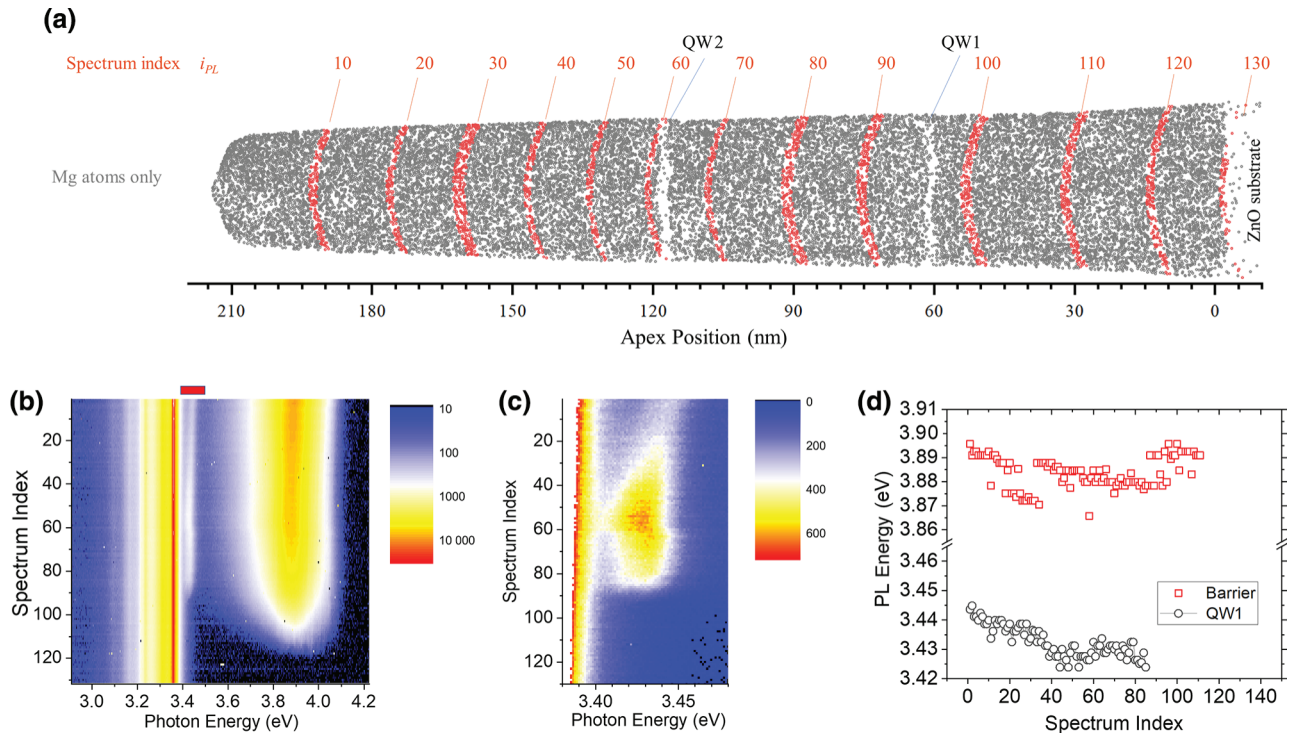


FIG. 5. (a) Slice extracted from the 3D reconstruction of the positions of Mg ions. Ions highlighted in orange correspond to those detected during acquisition of the PL spectrum indexed by  $i_{\text{PL}}$ . (Notably, only volumes collected during the 10th, 20th, 30th, etc. spectra are shown in this way and serve as a guide to the eye.) (b) Sequence of PL spectra acquired during evaporation of the field emitter. Red bar indicates the spectral region corresponding to the QW1 emission, i.e., to the magnification shown in (c). (d) PL energy of the (Mg,Zn)O barrier (red squares) and QW1 (black circles) as a function of the spectrum index  $i_{\text{PL}}$ .

Referring to Fig. 5(b) and the plot of Fig. 5(d), in which the maximum energies of the (Mg, Zn)O and QW1 peaks are reported as a function of  $i_{\text{PL}}$ , it is clear that the energies of both peaks evolve during the analysis. The energy of QW1 steadily decreases, with the exception of a local increase after  $i_{\text{PL}} = 60$ . The local blueshift that both peaks experience at  $i_{\text{PL}} = 60$  correlates well with the local decrease of  $V_{\text{dc}}$  and of the surface electric field corresponding to the evaporation of QW2, as reported in Fig. 3(b). The occurrence of this local blueshift will be explained in detail in the discussion Sec. V. The energy of the barrier emission also exhibits changes, but, as this emission is due to the superposition of dipoles distributed along tens of nanometers, its interpretation is not straightforward.

Focusing on the QW1 emission, the plot in Fig. 5(d) shows that its maximum energy changes from  $E = 3.445$  eV at the beginning of evaporation to  $E = 3.425$  eV shortly before the evaporation of QW1: the peak thus undergoes a redshift of  $\Delta E_1 = -20$  meV during the analysis (the shift of the average is slightly lower due to the superposition of the ZnO peak tail). The total redshift from the beginning of the voltage ramp amounts, altogether, to  $\Delta E_1 = -30$  meV. The PL of QW1 is completely suppressed for  $i_{\text{PL}} = 88$ . A comparison with the reconstructed volume shown in Fig. 5(b) indicates that the loss of the PL signal takes place when the apex is at a maximum distance of around 10 nm from the QW1 region. This could be due to either the fact that the actual emitting dipoles are not close to the axis in the APT field of view or to the increase of stress at the proximity of the apex—to be quantified in the following—which may induce the migration of nonradiative point defects towards QW1.

It should be noted that both (Mg, Zn)O and QW1 peak intensities vary throughout the analysis. This behavior is most likely related to the shape evolution of the field emitter and to the variation of the dielectric environment of the emitting dipoles. However, this phenomenon constitutes *per se* the object of a different study and will not be treated in this work.

The energy shifts of the PL emission can be interpreted through the effect of strain within the field emitter. This requires the theory of strain within a field emitter in an electrostatic field, which constitutes the focus of the next section, to be set down.

#### IV. STRESS, STRAIN, AND BAND-GAP EVOLUTION IN AN EVAPORATING FIELD EMITTER

These experimental results can be interpreted through the theory of linear elasticity in semiconductors and through strain-dependent band theory [33]. While this theory is proven to be useful in the study of nanowires [14,34],

it has not been applied, so far, to field emitters that change shape during evaporation. This constitutes the object of the present section.

Stress and strain may build up in a field emitter via two distinct mechanisms:

(i) *A structural mechanism*, i.e., the presence of built-in strain due to the presence of coherent heterostructure interfaces. Due to the nanoscale dimensions of the system, this built-in strain can elastically relax at the field-emitter surfaces. Relaxation is more effective when the lateral dimensions of the tips are smaller, i.e., the phenomenon depends on the geometric shape of the system. A similar situation is found in nanowire axial [35] and radial [36] heterostructures.

(ii) *An environmental mechanism*, i.e., the application of an electrostatic potential at the tip, translating into an electrostatic field at the tip apex. This field induces an electrostatic stress that propagates into the tip volume in a way that depends on its geometric shape [26].

For the sake of clarity, in the following, we make three simplifying assumptions:

(a) The strain-related energy shifts observable in the exciton recombination yielding the PL signal of the quantum well are determined by the action of strain on the ZnO bands only. In other words, we assume that strain affects the recombination energy via its effect on the band-gap energy of the highest valence bands (or, equivalently, on the lowest exciton energy). The possible effect on the alignment of the ZnO and (Mg, Zn)O bands is shown to be negligible [22]. The effect on the QW confinement energy is also expected to be negligible versus the band-gap shift.

(b) The ZnO/(Mg, Zn)O QW-barrier system can be described as a set of planar interfaces between homogeneous phases. Despite APT clearly showing that this is not the case, as the QW-barrier interface has a groove profile and decomposition phenomena take place within the barriers, this approximation can be shown to be tenable. We will indeed show in the following that the main agent responsible for the PL energy shift of the QW observed during the PAP analysis is the applied electric field. Furthermore, the effect of decomposition in (Mg, Zn)O would result only in some dispersion of strain and stress values in the neighborhood of the same trends that a random alloy would exhibit.

(c) The optically active region lies close to the axis of the field emitter. This assumption is justified by the fact that FIB preparation introduces nonradiative recombination centers over a distance of several tens of nanometers from the surface [37]. Interpretation of the experimental results is then performed based on the quantities calculated along the axis of the field emitter.

### A. General relationships

The stress and strain tensors  $\vec{\sigma}$  and  $\vec{\varepsilon}$  are linearly dependent via the stiffness matrix  $C$  containing the elastic constants of the material:

$$\vec{\sigma} = C\vec{\varepsilon}. \quad (1)$$

The numerical values of the elastic constants relative to ZnO and (Mg, Zn)O are given in the Appendix.

The effect of strain on the band energies can be determined by solving the eigenvalue problem of the  $\mathbf{k}\cdot\mathbf{p}$  effective mass Hamiltonian at the  $\Gamma$  point of the Brillouin zone, defined in the quasicubic model for II-VI wurtzite semiconductors [33], also adopted in Refs. [38,39]:

$$H = H(\vec{\varepsilon}).$$

The strain-induced energy shift is then calculated as the variation of the energy gap of ZnO with respect to its strain-free state. Notably, this does not consider the effect of strain on the confinement energy. This approximation will be justified *a posteriori* in the Sec. V dealing with the limitations of the model.

As outlined in more detail within the Appendix, the strain Hamiltonian contains both constant terms relative to the unperturbed band structure and strain-dependent terms. These are determined by the set of deformation potentials of ZnO [33,38]. It should be noted that a corresponding set of deformation potentials have not been determined yet for (Mg, Zn)O with an arbitrary Mg content.

It must also be underlined that stress and strain are linearly dependent, so the components of the strain tensor induced by an electrostatic stress add up to the components related to lattice mismatch or surface relaxation. However, the eigenvalues of the  $H(\vec{\varepsilon})$  Hamiltonian are, in general, not linearly dependent on the strain components. It is thus the total strain that must be fed into  $H(\vec{\varepsilon})$  in order to accurately calculate the energy shift resulting from the superposition of different stress or strain sources.

### B. Lattice-mismatch-induced strain

In a ZnO quantum well grown epitaxially on the  $m$  plane, strain can build up due to lattice mismatch along the  $a$  and the  $c$  axes (here identified by the  $y$  and  $z$  directions, respectively). If  $\varepsilon_{yy}$  and  $\varepsilon_{zz}$  of the strain tensor are given, the on-axis component,  $\varepsilon_{xx}$ , is then found by

$$\varepsilon_{xx} = -\frac{c_{12}\varepsilon_{yy} + c_{13}\varepsilon_{zz}}{c_{11}}, \quad (2)$$

where  $c_{ij}$  are the components of the stiffness matrix  $C$ . Keeping this relationship under consideration, the expected shift of the lowest exciton energy,  $E_1$ , is visualized in the plot of Fig. 6(a). However, the strain relationship for a ZnO

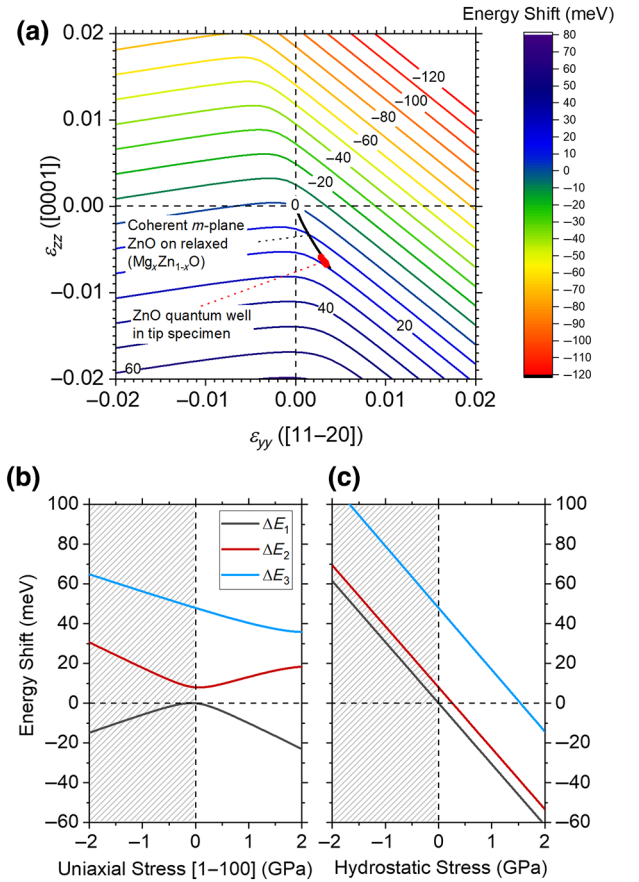


FIG. 6. Strain and stress effects on the exciton energies in ZnO. (a) Relationship between the in-plane strain tensors of a coherently strained ZnO film epitaxially grown on the  $m$  plane and the energy shift of the lowest exciton level. Black line represents the strain state of a coherent  $m$ -plane ZnO layer epitaxially grown on relaxed  $\text{Mg}_x\text{Zn}_{1-x}\text{O}$  ( $x < 0.35$ ). Red spot indicates the strain state calculated for the ZnO QW contained within the field-emission tip. (b) Energy shifts of three ZnO exciton bands as a function of uniaxial stress directed along the  $m$  direction [1 $\bar{1}$ 00]. (c) Energy shift of three ZnO exciton levels as a function of hydrostatic stress. Gray-shaded regions correspond to compressive stress, which is not applicable in the present experiment.

QW epitaxially grown on (Mg, Zn)O must comply with specific constraints.

ZnO and (Mg, Zn)O do not possess the same lattice constants. Under the hypothesis that there are no decomposition or phase separation phenomena in (Mg, Zn)O, the lattice constants can be expressed as a function of the II-site Mg fraction,  $x_{\text{Mg}}$ , as follows [40]:

$$a(x_{\text{Mg}}) = (3.2459 + 0.012 x_{\text{Mg}} + 0.09 x_{\text{Mg}}^2) \text{ \AA}, \quad (3)$$

$$c(x_{\text{Mg}}) = (5.2126 - 0.076 x_{\text{Mg}} - 0.142 x_{\text{Mg}}^2) \text{ \AA}. \quad (4)$$

It is remarkable that in (Mg, Zn)O the lattice is deformed in a highly anisotropic way, as it expands on the

basal plane and it contracts along the polar  $c$  axis of wurtzite with increasing Mg content. In the present work, the ZnO/(Mg, Zn)O interfaces are approximately defined along the  $m$  plane. A coherent ZnO/(Mg, Zn)O interface is therefore characterized by strains of opposite signs along the  $y$  and  $z$  (i.e.,  $a$  and  $c$  in the WZ system) directions on the plane. According to relations (3) and (4), a ZnO QW coherently strained on relaxed (Mg, Zn)O with  $x_{\text{Mg}} < 0.32$  has a strain state spanning the black line traced in Fig. 6(a).

### 1. Properties in a tip with constant shape

The thin-film samples grown by MBE for this study are designed to support pseudomorphic growth of the (Mg, Zn)O layer. In other words, (Mg, Zn)O acquires the same lattice constants of ZnO on the  $m$  plane, and it slightly adapts its lattice constant along the  $m$  axis to minimize the elastic energy. In this pseudomorphic thin-film configuration, the ZnO QWs have, thus, the same lattice parameters of the ZnO substrate and the band-gap shift would be zero.

The results of the strain calculation performed within the elastic energy-minimization algorithm implemented by

the NEXTNANO<sup>++</sup> solver [41] on the geometry of the studied tip and reported in Figs. 7(a) and 7(b) for the tip before evaporation shows that the situation is radically different in field emitters. In the studied system, the interlayer distance and extension of the region of interest are comparable with the radius of the cross section of the tip. In this situation, strain relaxes effectively at lateral surfaces. The (Mg, Zn)O barrier is strained on ZnO (actually only partially, as it mutually strains the ZnO substrate), but it relaxes to its unperturbed lattice parameters between QW1 and QW2. QW1 is thus very close to the situation of ZnO coherently strained on relaxed (Mg, Zn)O. The stress state is calculated through the application of Eq. (1) to the strain maps, as reported in Figs. 7(a) and 7(b), showing that stresses in the order of GPa can build up along the interface planes. Consistently with relations (3) and (4),  $\varepsilon_{yy}$  and  $\sigma_{yy}$  are positive, while  $\varepsilon_{zz}$  and  $\sigma_{zz}$  are negative. As the tip is free to relax in the  $x$  direction, the  $\sigma_{xx}$  component of the stress tensor is nearly zero. The energy shift of the lowest exciton level is calculated by applying the  $H(\vec{\varepsilon})$  Hamiltonian on the strain maps, as reported in Fig. 7(d). The exciton energy in QW1 undergoes a blueshift of around 16 meV.

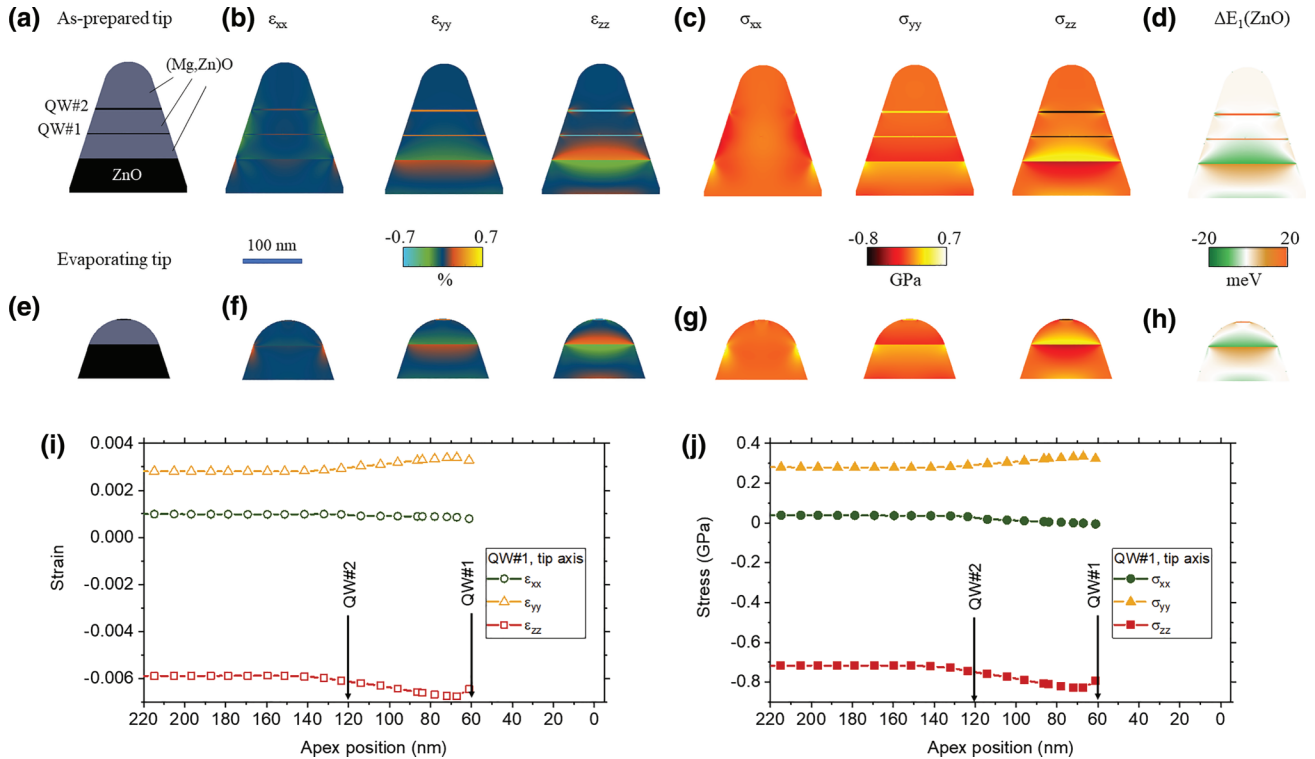


FIG. 7. Strain-stress states related to lattice mismatch and their evolution in the field emitter containing the ZnO/(Mg, Zn)O heterostructure. Field emitter before evaporation: (a) scheme of the materials system, (b) components of the strain tensor, (c) components of the stress tensor and (d) expected shift of the lowest ZnO exciton level. (e)–(h) correspond to (a)–(d) for the situation in which the apex of the field emitter is in close proximity to QW1 after partial evaporation. (i) Evolution of strain components at the center of QW1 as a function of the apex position. (j) Evolution of the stress components at the center of QW1 as a function of the apex position.

## 2. Evolution of stress, strain, and band gaps in an evaporating tip

When the field emitter evaporates, its shape gradually transforms into that schematically shown in Figs. 7(e)–7(h). This is a sort of snapshot of the tip shape just before the evaporation of QW1. The strain and stress components for this configuration are visualized in the 2D color plots in Figs. 7(f) and 7(g). What can be noticed from these plots is that the strain due to lattice mismatch at the ZnO substrate-(Mg,Zn)O interface relaxes more effectively due to the modified shape of the tip. As a result, QW1 will be lying on almost completely relaxed (Mg,Zn)O. The strain and stress state at the center of QW1 varies as a consequence of this relaxation and is quantitatively reported in Figs. 7(i) and 7(j). From both strain and stress trends, it appears that the variation of the strain and stress state is small, but not negligible. The relative change in the strain or stress state for the  $yy$  and  $zz$  in-plane components may be up to 20% during the experiment. The in-plane strain state of QW1 is also reported in the red spot in Fig. 6(a). Interestingly, the modification begins to take place effectively upon the evaporation of the upper QW2, which is reasonable, as any ZnO inclusion within the (Mg,Zn)O matrix has the effect of inhibiting the relaxation of the latter. If we neglect the effect of the applied bias (which will be treated in the next section), the energy shift of the lowest exciton energy varies from 16 to 19 meV, as reported through the blue dotted line in Fig. 8.

As a concluding remark for this section, these results are related to the tip geometry, heterostructure configuration,

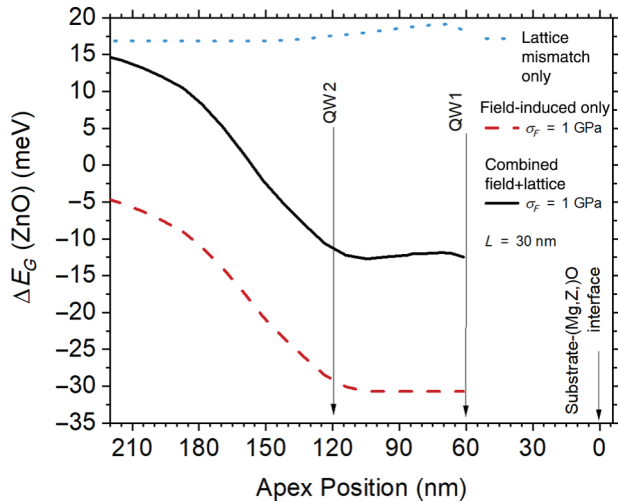


FIG. 8. Energy shifts calculated as a function of the apex position in the evaporating field emitter. Blue dotted line corresponds to the shift related to lattice mismatch, neglecting the effect of the applied field. Red dashed line corresponds to the shift related to the applied bias, neglecting the effect of lattice mismatch. Black solid line corresponds to the shift resulting from the combined effect of lattice mismatch and applied bias.

and crystal orientation specific to this study. Calculations performed on other tip geometries—not shown—indicate that modification of the energy shift decreases with decreasing tip radius, which may be easily understood due to the proximity of the lateral surfaces assisting relaxation of the (Mg,Zn)O lattice at short distances from the interface with the ZnO substrate. Considering all of these parameters, the effect of lattice relaxation during tip evaporation may thus be larger in other systems.

## C. Field-induced strain

The problem of stress induced by the voltage applied to a field-emission tip has been thoroughly discussed in a previous study [26]. The intensity of the electric field,  $F_s$ , present at the apex surface can be related to the apex radius,  $R_{\text{apex}}$ , of the needle and to the applied bias,  $V_{\text{dc}}$ :

$$F_s = \frac{V_{\text{dc}}}{k_f R_{\text{apex}}}, \quad (5)$$

where  $k_f$  is a geometric factor that depends on the tip shank angle and on its electrostatic environment [42]. Due to the accumulation of a high density of valence-band holes on the apex surface [43], the field induces Maxwell stress on the apex surface:

$$\sigma_F = \frac{1}{2} \epsilon_0 F_s^2. \quad (6)$$

At constant geometry, apex stress (and linearly related strain) is thus proportional to the square of the field and, through Eq. (5), to the square of the applied voltage. Concerning the electric field, we assume that it can be considered as being completely screened in the tip within the first nanometer from the surface, as supported by calculations and the experimental observations reported in Ref. [43].

### 1. Properties in a tip with constant shape

Approximating the apex as a hemisphere and integrating the forces  $d\mathbf{T}$  that develop on a surface element  $dS$ , the resultant tension  $\mathbf{T}$  along the needle axis is

$$\mathbf{T} = \pi R_{\text{apex}}^2 \sigma_F \hat{\mathbf{n}}_{[1\bar{1}00]} \quad (7)$$

where  $\hat{\mathbf{n}}_{[1\bar{1}00]}$  is a unit vector pointing along the  $[1\bar{1}00]$  crystal direction aligned with the tip axis for the particular system studied herein. The stress at the apex itself is hydrostatic, as the Maxwell forces are directed approximately along the needle radius. At a distance from the apex equal to several  $R_{\text{apex}}$ , there is a transition from hydrostatic to uniaxial stress, acting on an axial cross section of the tip

that is uniaxial. This transition is described in an analytical approximation as follows:

$$\sigma_{xx}(x) = |\mathbf{T}|/S(x), \quad (8)$$

$$\sigma_{yy}(x) = \sigma_{zz}(x) = \sigma_{xx}(x) \exp\left(\frac{x - x_i}{L}\right),$$

where

$$S(x) = \pi R(x)^2, \quad (9)$$

is the area of the axial cross section at coordinate  $x$ , and  $x_i$  is the coordinate of the interface between the hemispherical and conical section of the tip. The coordinate  $x_i$  decreases as evaporation progresses. The transition length  $L$  is *a priori* not known, because it depends not only on the geometry of the tip, but also on the actual value of the field on the conical section, which is nonzero. In principle, the field could be calculated everywhere on the tip, then the stress could be calculated with, e.g., a finite-element approach. However, this approach is more complex and would be

less transparent than the adopted analytical approximation. The transition length  $L$  can, in any case, be treated as a sort of fitting parameter, as shown in the discussion Sec. V. The strain state is then calculated by the application of the inverse of the  $C$  matrix [Eq. (1)] on the stress maps. The trends of strain and stress components in the actual tip geometry are reported in Figs. 9(b) and 9(c), respectively, for an apex stress of  $\sigma_F = 1$  GPa. The maps are traced for a transition length  $L = 50$  nm, which is in the order of the apex radius before evaporation. This value is unrealistically small, but it is suitable for visualization purposes.

The effect of uniaxial stress directed along the  $m$  axis and that of hydrostatic stress on the three ZnO exciton energies are reported in Figs. 6(b) and 6(c) respectively, showing that, for an apex tensile stress strength of 1 GPa, redshifts of around  $-10$  and  $-30$  meV are expected in the case of uniaxial and hydrostatic stress, respectively. The energy shift in the tip geometry, calculated with the  $H(\varepsilon)$  Hamiltonian, is reported in Fig. 9(d). The apex stress induces a redshift of around  $-30$  meV in the proximity of the apex (i.e., in the region included in the hemispherical region

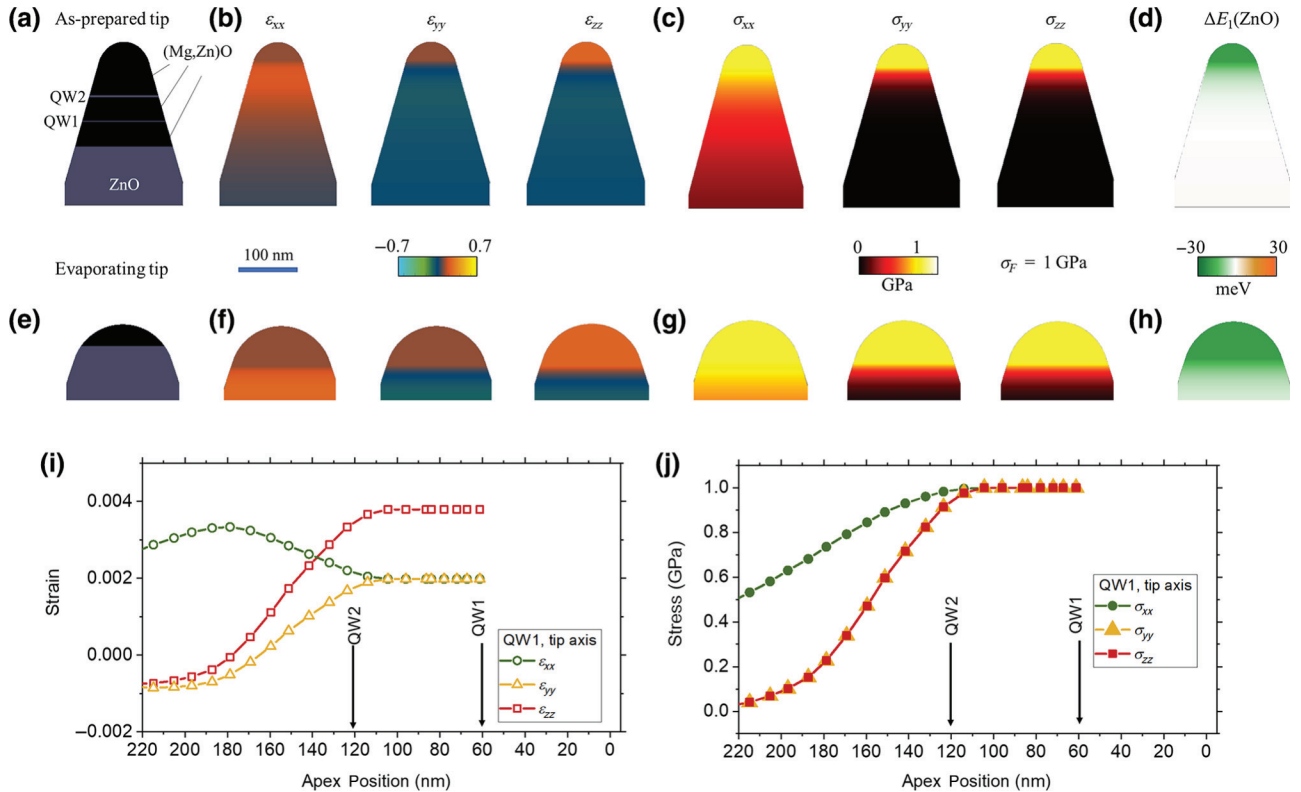


FIG. 9. Strain-stress states related to the application of an electric field at the apex and their evolution in the field emitter containing the ZnO/(Mg, Zn)O heterostructure. Apex stress is set at 1 GPa, while hydrostatic-uniaxial stress transition length  $L$  is set at  $L = 30$  nm. Field emitter before evaporation: (a) scheme of the materials system, (b) components of the strain tensor, (c) components of the stress tensor, and (d) expected shift of the lowest ZnO exciton level. (e)–(h) correspond to (a)–(d) for the situation in which the apex of the field emitter is in close proximity to QW1 after partial evaporation. (i) Evolution of the strain components at the center of QW1 as a function of apex position. (j) Evolution of the stress components at the center of QW1 as a function of apex position.

close to the apex) where the stress is hydrostatic. The exciton energy shift, calculated in the absence of lattice-mismatch-related effects, gradually decreases towards the interior of the tip due to the increase of its cross section and to the transition to uniaxial stress.

For a tip with constant geometry, the strain-stress relationships are linear. So, in every point of the tip, stress and strain are proportional to the square of the surface field,  $F_s$ , and of the applied voltage,  $V_{dc}$ .

## 2. Evolution of stress, strain, and band gaps in an evaporating tip

The components of the stress tensor induced at the center of QW1 by a constant electric field applied to the tip apex are reported in Fig. 9(c) as a function of the distance of the apex from the (Mg, Zn)O/ZnO substrate interface for the tip structure shown in Fig. 9(a). The corresponding components of the strain tensor at the center of QW1 are visualized in Fig. 9(b). These plots illustrate the dynamic evolution of the mechanical state of QW1 during evaporation of the tip.

The reported data indicate that strain induced by the applied field within QW1 increases as the apex approaches. This happens because the applied field remains constant (approximately constant in the actual experiment), but it is applied to a larger and larger apex as the tip evaporates. In this way, the total mechanical tension on the tip increases during its evaporation. It should be noted that the largest strain component is  $\varepsilon_{xx}$  when the stress is uniaxial, while it becomes  $\varepsilon_{zz}$  when the stress becomes hydrostatic close to the tip apex.

The expected energy shift of the lowest exciton energy, calculated without considering any other strain sources, is reported as the red dashed line in Fig. 8 for an apex stress of  $\sigma_F = 1$  GPa, corresponding to an apex field of  $F_s = 15$  V/nm. The shift varies from around  $-8$  meV to around  $-30$  meV from the beginning of the experiment until evaporation of the QW1 layer. At this apex stress strength, the effect of field-induced stress and its modification during evaporation are significantly larger than the energy modification related to relaxation of the lattice during evaporation.

## D. Combined effect of lattice-mismatch-related and field-induced band shifts

The combined effect of lattice-mismatch-related and field-induced shifts of the lowest exciton energy is shown by the black solid line in Fig. 8 for an assumed apex stress of 1 GPa and a transition length of  $L = 30$  nm. The energy shift resulting from the combination of the two mechanisms is not exactly a linear combination of the two separately considered shifts, but it is quite close to it. It can be noted that the trend of the combined shift qualitatively reproduces the trend of the energy shift related to the effect

of the field during evaporation. The lowest exciton energy undergoes a shift varying from 15 to  $-11$  meV.

## V. CORRELATION OF MODEL AND EXPERIMENT

### A. Interpretation of the energy shifts of quantum-well luminescence

#### 1. Determination of apex stress and electric field

The shift observed in the PL energy of QW1 can be interpreted as being due to its varying strain state both as a function of the applied voltage when its geometry is constant and as a function of the evaporated volume while it is evaporating during APT analysis. The model developed in Sec. IV allows us to calculate the expected spectral shifts on the actual tip geometry.

Figures 10(a)–10(d) represent a synthetic view of experimental data of the peak energy of QW1 (a),(c) as a function of the applied bias during the voltage ramp (b),(d) and as a function of the apex position during evaporation. In Figs. 10(a) and 10(b), experimental data are compared with predictions obtained through calculations for different values of the apex stress,  $\sigma_F$ , and with a fixed hydrostatic-uniaxial stress transition length of  $L = 150$  nm. The position of the calculated shift with zero stress is translated on the energy scale in order to match the PL energy of the unperturbed QW1 (i.e., contained in the tip when  $V_{dc} = 0$ ).

In Fig. 10(a), experimental data are compared with the calculation of the expected shift at QW1 when an increasing stress,  $\sigma_F^{\text{ramp}}(V_{dc})$ , is applied during the voltage ramp. This stress then stabilizes at  $\sigma_F$ . The relationship between the stress,  $\sigma_F^{\text{ramp}}$ , and voltage is simply given by

$$\sigma_F^{\text{ramp}}(V_{dc}) = \sigma_F \left( \frac{V_{dc}}{V_{e,s}} \right)^2, \quad (10)$$

where  $V_{e,s} = 6$  kV is the voltage where evaporation “starts,” i.e., yields the detection rate set for the experiment. In Fig. 10(b), the PL energy during evaporation can be compared with different shifts expected for different apex stresses. Considering both voltage ramp and evaporation, it is apparent that the best approximation of the overall shift (i.e., from the absence of field to the situation in which QW1 is close to evaporation) is given by the assumption of an apex stress of  $\sigma_F = 1.25$  GPa. This value corresponds to an apex surface field of  $F_s = 16.8$  V/nm, which is very close to the value assumed for the reconstruction algorithm, and is consistent with the microscopic field value of  $F_\mu \sim 20$  V/nm inferred from the charge-state analysis. We notice, however, that, for  $\sigma_F = 1.25$  GPa and  $L = 150$  nm, the PL behavior during the ramp is not best reproduced. The ramp is best fitted by the parabola with  $\sigma_F = 1.5$  GPa. However, this stress value predicts a larger redshift than that experimentally observed. This

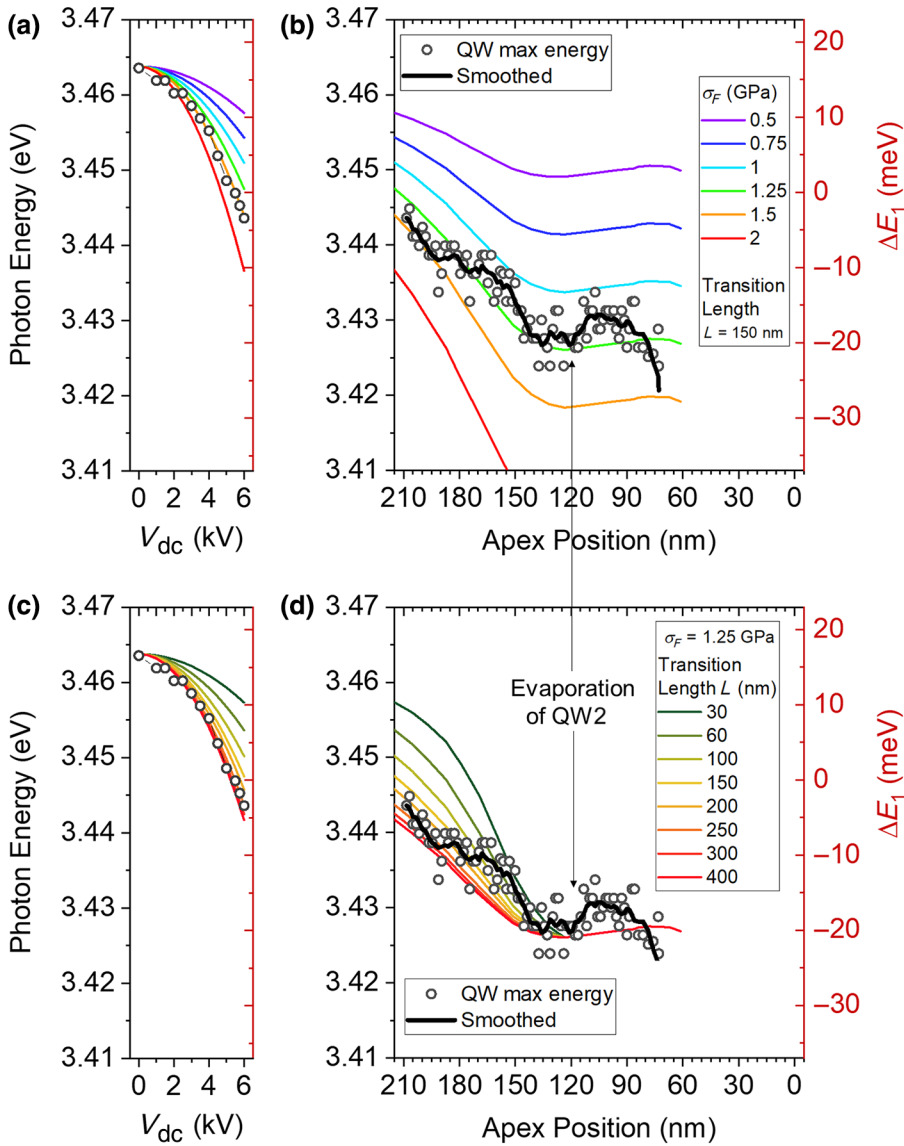


FIG. 10. Comparison between calculated and experimental energy shifts. (a) Experimental and calculated PL energies during the voltage ramp as a function of applied bias  $V_{dc}$  and (b) as a function of apex position during field-emitter evaporation calculated for different apex stress levels and for a fixed hydrostatic-uniaxial stress transition length  $L = 150$  nm. (c),(d) Same as in (a),(b), but calculations are performed for fixed apex stress  $\sigma_F = 1.25$  GPa and varying values of  $L$ .

apparent discrepancy is related to the assumption about the hydrostatic-uniaxial stress transition length.

The effect of the hydrostatic-uniaxial stress transition length,  $L$ , is shown in Figs. 10(c) and 10(d). The different calculated curves relate to an apex stress during evaporation of  $\sigma_F = 1.25$  GPa, while  $L$  is allowed to vary. It appears clearly that the curves best fit the PL shift during the voltage ramp in Fig. 10(c) when  $L > 200$  nm, i.e., assuming a hydrostatic stress reaching QW1. It is clear that, for values of  $L$  larger than the actual QW1 distance from the apex at the beginning of evaporation, the strain state only weakly depends on  $L$  at the QW1 position. It is thus not possible to draw a quantitative conclusion about  $L$ , but a lower limit of  $L = 200$  nm can be set. This behavior is most probably related to the presence of a residual surface field at the surface of the conical part of the tip, a field that is not sufficiently intense for promoting evaporation, but which still has non-negligible mechanical effects.

It can also be underlined that this conclusion is consistent with the results obtained in previous studies, in which splitting of the zero-phonon lines of the PL of the color centers in diamond are studied [26,27]. In these studies, it was possible to measure the apex stress under the hypothesis that the stress was uniaxial. Also, the distances of the emitting centers from the apex were significantly larger, up to several microns, so it would not be reasonable to expect hydrostatic stress.

## 2. Optical sensing of field variation

Calculations performed according to the model do not consider variation in the surface field that occurs when QW2 is evaporated. This variation is now discussed in more detail. According to the voltage curve [Fig. 3(b)], the relative difference in the applied voltage implies a similar relative difference in the surface

field,  $|\Delta V_{dc}/V_{dc}| = |\Delta F_s/F_s| \approx -4\%$ , during the evaporation of QW2. Comparing the local increase in the QW1 PL energy with the calculations reported in Fig. 10(b), we can estimate that just after the evaporation of QW2 the stress decreased from 1.25 GPa to around 1.1–1.15 GPa, with a relative difference of  $|\Delta\sigma_F/\sigma_F| \approx 12\%$ – $8\%$ , which is reasonably close to the expected value of  $|\Delta\sigma_F/\sigma_F| \approx 2|\Delta F_s/F_s|$  obtained from quadratic relation (6).

The important point about this phenomenon is that QW1 senses the evaporation of QW2. The use of a PAP makes it possible to establish a sort of strain coupling of these two wells via the action of the surface electric field. The evaporation of QW2 leaves a trace on the behavior of QW1. Clearly, this also depends on the fact that the experiment is performed at a constant detection rate. However, it is possible to imagine that closer QWs would exhibit a stronger strain interaction: this would be related to relaxation of the lattice-related strain during evaporation, because the amount of evaporated volume of the upper-lying QW would have a larger impact on the strain state of the lower-lying QW. This opens up interesting possibilities for the study of the optical properties of quantum-confined emitters by the PAP.

Finally, it is worth mentioning that the mechanical tension on the tip increases during its evaporation. Also, stress exerted at the base of the tip, where it is usually soldered to a larger tip-shaped support, increases during the experiment. If the base is not sufficiently large or properly soldered, this increase may be the origin of specimen failure in APT analysis of soldered specimens, which are analyzed with an approximately constant surface field throughout the experiment.

## B. Limitations of the current approach

To conclude the discussion section, it is worth clarifying the main limitations of the results presented herein. There are indeed both experimental and theoretical limitations that can possibly be overcome in the near future.

### 1. Experimental limitations

From the experimental point of view, the current setup is limited to a geometrical field of view of the ion detector of around  $\pm 8^\circ$ . This makes it possible to image a quantum well within a heterostructure at the correct depth, but it excludes a large part of its volume. As carrier localization is an important phenomenon in these systems [44–46], carriers may localize outside the field of view of the APT. This may also be the reason why the QW1 luminescence quenches some 10 nm before the apex reaches it on the axis, i.e., before it completely evaporates. This limit can be relaxed through technical intervention on the instrument. Increasing the field of view will be highly beneficial for the study of pointlike light emitters, such as quantum dots

or color centers. A deeper insight can indeed be reached if it is possible to compare the full 3D chemical image of the light emitter with its optical signature. Another point concerns the effective measurement of the tip shape, which is known to deviate from that of a cone surmounted by a portion of a sphere or ellipsoid in the case of the evaporation of layers with significantly different evaporation fields [47]—this possibility may apply to specific QW systems. It would be interesting to know the shape of the tip (particularly its apex radius) exactly during evaporation. This would require a much more demanding approach, with the implementation of a PAP coupled with a transmission electron microscope.

Finally, we notice that electrostatic stress can be applied as a tensile stress only (changing the sign of the bias does not change the sign of the stress, not to mention that the onset of electron-field emission would occur well before reaching the field intensities typical of ion emission). However, the method presented here is an original way to implement tensile-strain-dependent measurements not only on top-down fabricated field emitters, but also on nanowires, which can be characterized by APT based on different preparation protocols [48]. An original optical path to strain-stress curves on nanoscale systems can be considered as being opened up.

### 2. Limitations of the model

Herein, we choose to perform calculations within a simplified theoretical framework, which is meant to convey the novelty of the results and the interplay of different physical aspects of the analyzed system. Among the main simplifying assumptions, we adopt several related to the strain model, in particular, the adoption of an analytical approximation to describe stress propagation within a field emitter. This limitation can be overcome by implementing finite-element calculations similar to those carried out for the lattice-mismatch-related stress (it should be mentioned that the solution of the stress-strain equations with boundary conditions at the tip surface is not implemented in the software package we use; furthermore, the determination of such boundary conditions is *per se* another problem [47]). The exciton energy shift is calculated based only on the strain effect on the ZnO band gap. The effect on the (Mg,Zn)O band gap is more difficult to determine because the deformation potentials for this material are not as well known as those for ZnO. More precise calculations can be achieved by considering the quantum confinement effect and possibly the wave-function symmetry. However, these calculations would be probably more precise, but it is likely that the effect of the evolution of the strain state on the confinement energies would not be particularly significant. Concerning the effect of strain on the confinement energy, for instance, we consider that the shift,  $\Delta E_g$ , of the ZnO band gap spans over around

30 meV, yielding a relative shift of  $\Delta E_g/E_g \sim 1\%$ . A similar relative shift should be set for the QW confinement energy, i.e.,  $\Delta E_{c,QW}/E_{c,QW} \sim 1\%$ . As  $E_{c,QW} = 0.1$  eV, this would correspond to a shift of the confinement energy of around  $\Delta E_{c,QW} \sim 1$  meV, which is lower than the level of fluctuation of the peak energy during the analysis. The field-induced variation of the strain state could also lead to modifications of the wave-function symmetry (such modifications are here somehow embedded in the strain dependence of the valence bands in the  $\mathbf{k}\cdot\mathbf{p}$  Hamiltonian, but this Hamiltonian refers to bulk properties, and quantum confinement effects could occur in the case of narrow QWs). Finally, an estimate, or a measurement, of the effective temperature of the quantum well would add useful information, also in terms of possible effects of the differences of lattice expansion of the heterostructure phases. These implementations are left for further and more specialized work.

## VI. CONCLUSIONS AND PERSPECTIVES

This work reports on the possibility of measuring stress, strain, and the intensity of the field applied to the apex of a field emitter through the application of a recently developed instrument, referred to as PAP, which couples APT and PL spectroscopy. We apply this correlative technique to the analysis of ZnO/(Mg,Zn)O quantum-well heterostructures. The PL signal of a QW is found to shift in energy as a function of the voltage applied to the field emitter. To explain this shift, we develop a strain model, taking into account the crystal orientation of the emitter, the dimension and position of the heterostructure interfaces, the composition of the (Mg,Zn)O alloy (despite correlative microscopy not being the main focus of this article, all of this information can be retrieved by APT analysis itself in a strictly correlative way through the unique features of the PAP), and the morphology of the field emitter. The strain model considers both strain related to the presence of coherent heterostructure interfaces and the effect of the application of an external bias. It becomes possible to predict the PL energy shifts both as a function of the voltage applied to the emitter and as a function of the evolution of its shape during APT analysis. A comparison of the calculations and experimental data makes it possible to determine the applied surface field, the corresponding stress, and the strain state within the tip itself. Here, the QW is exploited as a localized probe capable of optically transducing variations of the environmental parameters that determine its spectral signature.

The application of the PAP is expected to have further implications in materials science and in the study of the physics of laser-matter interactions in field emitters under high field. Stress-dependent (piezospectroscopic) optical measurements can, for instance, be applied to the determination of deformation potentials in materials in which

they are not known. The strain coupling of neighboring quantum emitters can also be studied. From this perspective, it would be interesting to perform stress-dependent spectroscopy on quantum dots containing functional impurities. The study of irreversible phenomena could also be achieved: stress-induced dislocation motion or diffusion of point defects within strain gradients could also influence the optical properties of localized emitters. Finally, the photonic coupling of the emitting dipoles to their environment (analyzable, for instance, through the PL intensity or through the evolution of a time-resolved PL signal) is another domain that can be addressed through the application of the photonic atom probe.

## ACKNOWLEDGMENTS

This work is funded by the French National Research Agency (ANR) in the framework of the projects EMC3 Labex AQRATE, EMC3 Labex IDEPOP, ANR-13-JS10-0001-01 TAPOTER, and ANR-11-EQPX-0020 GENESIS and co-funded in the framework of RIN IFROST, EMC3 Labex IDEPOP, and CPER BRIDGE projects by the European Union with the European Regional Development Fund (ERDF) and by Region Normandie. The authors from CRHEA also acknowledge funding from the EU Commission through the ZOTERAC project. E. Monroy and I. Dimkou are kindly acknowledged for fruitful discussion.

## APPENDIX: STRAIN HAMILTONIAN AND MATERIAL PARAMETERS

For the calculation of strain-dependent energy states, we adopt the formalism of Ref. [39], using the model of Langer *et al.* [33]. The three valence-band energies can be determined as the eigenvalues of the following Hamiltonian:

$$H = \begin{bmatrix} \Lambda_1 & \delta_3 & 0 \\ \delta_3 & \Lambda_2 & \sqrt{2}\Delta_3 \\ 0 & \sqrt{2}\Delta_3 & \Lambda_3 \end{bmatrix}, \quad (\text{A1})$$

where the quantities are

$$\begin{aligned} \Lambda_1 &= \Delta_1 + \Delta_2 + \delta_1 + \delta_2, \\ \Lambda_2 &= \Delta_1 - \Delta_2 + \delta_1 + \delta_2, \\ \Lambda_3 &= \delta_1, \end{aligned} \quad (\text{A2})$$

$$\begin{aligned} \delta_1 &= D_1 \varepsilon_{zz} + D_2 (\varepsilon_{xx} + \varepsilon_{yy}) - a_c, \\ \delta_2 &= D_3 \varepsilon_{zz} + D_4 (\varepsilon_{xx} + \varepsilon_{yy}), \\ \delta_3 &= D_5 (\varepsilon_{xx} - \varepsilon_{yy}), \end{aligned} \quad (\text{A3})$$

where  $\Delta_1$  is the wurtzite crystal field splitting,  $\Delta_2$  and  $\Delta_3$  represent the spin-orbit coupling, and  $\delta_i$  relates the strain to the unperturbed valence-band energy via the deformation potential  $D_i$ .

TABLE II. Material parameters used in the calculations.

Parameter	Symbol	ZnO	Mg <sub>0.27</sub> Zn <sub>0.63</sub> O	Ref.
Lattice constants	$a$	3.246 Å	3.256 Å	[40]
	$c$	5.213 Å	5.182 Å	[40]
Elastic constants	$C_{11}$	238 GPa	238 GPa	[40]
	$C_{12}$	106 GPa	106 GPa	[40]
	$C_{13}$	84 GPa	85.1 GPa	[40]
	$C_{33}$	176 GPa	177.5 GPa	[40]
	$C_{44}$	58 GPa	58 GPa	[40]
Band gap	$E_g$	3.441 eV	3.891 eV	[40]
Valence-band parameters	$\Delta_1$	-0.0383 eV	...	[38]
	$\Delta_2$	0.0021 eV	...	[38]
	$\Delta_3$	0.0091 eV	...	[38]
Deformation potentials	$D_1$	-3.9 eV	...	[38]
	$D_2$	-4.13 eV	...	[38]
	$D_3$	-1.15 eV	...	[38]
	$D_4$	1.22 eV	...	[38]
	$D_5$	1.53 eV	...	[38]
	$a_c$	-3.418 eV	...	[38]

The material parameters used for the calculations are given in Table II.

- [1] M. J. Hÿtch, E. Snoeck, and R. Kilaas, Quantitative measurement of displacement and strain fields from HREM micrographs, *Ultramicroscopy* **74**, 131 (1998).
- [2] M. Hÿtch, F. Houdellier, F. Hÿe, and E. Snoeck, Nanoscale holographic interferometry for strain measurements in electronic devices, *Nature* **453**, 7198 (2008).
- [3] H. Chen, R. M. Feenstra, R. S. Goldman, C. Silfvenius, and G. Landgren, Strain variations in InGaAsP/InGaP superlattices studied by scanning probe microscopy, *Appl. Phys. Lett.* **72**, 1727 (1998).
- [4] P. Offermans, P. M. Koenraad, J. H. Wolter, K. Pierz, M. Roy, and P. A. Maksym, Atomic-scale structure and photoluminescence of InAs quantum dots in GaAs and AlAs, *Phys. Rev. B* **72**, 165332 (2005).
- [5] G. Wedler, C. M. Schneider, A. Trampert, and R. Koch, Strain Relief of Heteroepitaxial Bcc-Fe(001) Films, *Phys. Rev. Lett.* **93**, 236101 (2004).
- [6] D. J. Weidner, M. T. Vaughan, L. Wang, H. Long, L. Li, N. A. Dixon, and W. B. Durham, Precise stress measurements with white synchrotron x rays, *Rev. Sci. Instrum.* **81**, 013903 (2010).
- [7] G. Martínez-Criado, J. Segura-Ruiz, B. Alén, J. Eymery, A. Rogalev, R. Tucoulou, and A. Homs, Exploring single semiconductor nanowires with a multimodal hard X-Ray nanoprobe, *Adv. Mater.* **26**, 7873 (2014).
- [8] I. Yeo, P.-L. de Assis, A. Gloppe, E. Dupont-Ferrier, P. Verlot, N. S. Malik, E. Dupuy, J. Claudon, J.-M. Gérard, A. Auffèves, G. Nogués, S. Seidelin, J.-P. Poizat, O. Arcizet, and M. Richard, Strain-mediated coupling in a quantum dot-mechanical oscillator hybrid system, *Nat. Nanotechnol.* **9**, 2 (2014).
- [9] L. Rigutti, G. Jacopin, L. Largeau, E. Galopin, A. De Luna Bugallo, F. H. Julien, J.-C. Harmand, F. Glas, and M. Tchernycheva, Correlation of optical and structural properties of GaN/AlN core-shell nanowires, *Phys. Rev. B* **83**, 155320 (2011).
- [10] G. Signorello, S. Karg, M. T. Björk, B. Gotsmann, and H. Riel, Tuning the light emission from GaAs nanowires over 290 MeV with uniaxial strain, *Nano Lett.* **13**, 917 (2013).
- [11] W. Shan, W. Walukiewicz, J. W. Ager, K. M. Yu, Y. Zhang, S. S. Mao, R. Kling, C. Kirchner, and A. Waag, Pressure-dependent photoluminescence study of ZnO nanowires, *Appl. Phys. Lett.* **86**, 153117 (2005).
- [12] N. Chauvin, A. Mavel, G. Patriarche, B. Masenelli, M. Gendry, and D. Machon, Pressure-dependent photoluminescence study of wurtzite InP nanowires, *Nano Lett.* **16**, 2926 (2016).
- [13] J.-Y. Kim, D. Jang, and J. R. Greer, Insight into the deformation behavior of niobium single crystals under uniaxial compression and tension at the nanoscale, *Scr. Mater.* **61**, 300 (2009).
- [14] G. Signorello, M. Schraff, P. Zellekens, U. Drechsler, M. Bürge, H. R. Steinauer, R. Heller, M. Tschudy, and H. Riel, An open-source platform to study uniaxial stress effects on nanoscale devices, *Rev. Sci. Instrum.* **88**, 053906 (2017).
- [15] J. Houard, A. Normand, E. Di Russo, C. Bacchi, P. Dalapati, G. Beainy, S. Moldovan, G. Da Costa, F. Delaroche, C. Vaudolon, J. M. Chauveau, M. Hugues, D. Blavette, B. Deconihout, A. Vella, F. Vurpillot, and L. Rigutti, A photonic atom probe coupling 3D atomic scale analysis with in situ photoluminescence spectroscopy, *Rev. Sci. Instrum.* **91**, 083704 (2020).
- [16] E. Di Russo, P. Dalapati, J. Houard, L. Venturi, I. Blum, S. Moldovan, N. Le Biavan, D. Lefebvre, M. Hugues, J. M. Chauveau, D. C. Blavette, B. Deconihout, A. Vella, F. Vurpillot, and L. Rigutti, Super-resolution optical spectroscopy of nanoscale emitters within a photonic atom probe, *Nano Lett.* **20**, 8733 (2020).
- [17] J.-M. Chauveau, M. Läggt, P. Venneguès, M. Teisseire, B. Lo, C. Deparis, C. Morhain, and B. Vinter, Non-polar-plane ZnMgO1/ZnO quantum wells grown by molecular beam epitaxy, *Semicond. Sci. Technol.* **23**, 035005 (2008).

- [18] I. Blum, F. Cuvilly, and W. Lefebvre-Ulrikson, in *Atom Probe Tomography* (Academic Press, Cambridge, MA, 2016), pp. 97–121.
- [19] L. Rigutti, A. Vella, F. Vurpillot, A. Gaillard, N. Sevelin-Radiguet, J. Houard, A. Hideur, G. Martel, G. Jacopin, A. D. Luna Bugallo, and B. Deconihout, Coupling atom probe tomography and photoluminescence spectroscopy: Exploratory results and perspectives, *Ultramicroscopy* **132**, 75 (2013).
- [20] K. Fisher and E. Marquis, Comparing plasma-FIB and Ga-FIB preparation of atom probe tomography samples, *Microsc. Microanal.* **22**, 692 (2016).
- [21] S. Du, T. Burgess, B. Gault, Q. Gao, P. Bao, L. Li, X. Cui, W. Kong Yeoh, H. Liu, L. Yao, A. V. Ceguerra, H. Hoe Tan, C. Jagadish, S. P. Ringer, and R. Zheng, Quantitative dopant distributions in GaAs nanowires using atom probe tomography, *Ultramicroscopy* **132**, 186 (2013).
- [22] E. Di Russo, L. Mancini, F. Moyon, S. Moldovan, J. Houard, F. H. Julien, M. Tchernycheva, J. M. Chauveau, M. Hugues, G. Da Costa, I. Blum, W. Lefebvre, D. Blavette, and L. Rigutti, Three-dimensional atomic-scale investigation of ZnO-Mg<sub>x</sub>Zn<sub>1-x</sub>O *m*-plane heterostructures, *Appl. Phys. Lett.* **111**, 032108 (2017).
- [23] D. Blavette, A. Bostel, J. M. Sarrau, B. Deconihout, and A. Menand, An atom probe for three-dimensional tomography, *Nature* **363**, 432 (1993).
- [24] B. Gault, F. Vurpillot, A. Vella, M. Gilbert, A. Menand, D. Blavette, and B. Deconihout, Design of a femtosecond laser assisted tomographic atom probe, *Rev. Sci. Instrum.* **77**, 043705 (2006).
- [25] G. D. Costa, H. Wang, S. Duguay, A. Bostel, D. Blavette, and B. Deconihout, Advance in multi-hit detection and quantization in atom probe tomography, *Rev. Sci. Instrum.* **83**, 123709 (2012).
- [26] L. Rigutti, L. Venturi, J. Houard, A. Normand, E. P. Silaeva, M. Borz, S. A. Malykhin, A. N. Obraztsov, and A. Vella, Optical contactless measurement of electric field-induced tensile stress in diamond nanoscale needles, *Nano Lett.* **17**, 7401 (2017).
- [27] L. Venturi, L. Rigutti, J. Houard, I. Blum, S. Malykhin, A. Obraztsov, and A. Vella, Strain sensitivity and symmetry of 2.65 eV color center in diamond nanoscale needles, *Appl. Phys. Lett.* **114**, 143104 (2019).
- [28] E. Di Russo, F. Moyon, N. Gogneau, L. Largeau, E. Giraud, J.-F. Carlin, N. Grandjean, J. M. Chauveau, M. Hugues, I. Blum, W. Lefebvre, F. Vurpillot, D. Blavette, and L. Rigutti, Composition metrology of ternary semiconductor alloys analyzed by atom probe tomography, *J. Phys. Chem. C* **122**, 16704 (2018).
- [29] D. R. Kingham, The post-ionization of field evaporated ions: A theoretical explanation of multiple charge states, *Surf. Sci.* **116**, 273 (1982).
- [30] L. Mancini *et al.*, Composition of wide bandgap semiconductor materials and nanostructures measured by atom probe tomography and its dependence on the surface electric field, *J. Phys. Chem. C* **118**, 24136 (2014).
- [31] F. Vurpillot, in *Atom Probe Tomography* (Academic Press, Cambridge, MA, 2016), pp. 183–249.
- [32] B. Laumer, F. Schuster, M. Stutzmann, A. Bergmaier, G. Dollinger, and M. Eickhoff, Accurate determination of optical bandgap and lattice parameters of Zn<sub>1-x</sub>Mg<sub>x</sub>O epitaxial films (0 ≤ x ≤ 0.3) grown by plasma-assisted molecular beam epitaxy on a-plane sapphire, *J. Appl. Phys.* **113**, 233512 (2013).
- [33] D. W. Langer, R. N. Euwema, K. Era, and T. Koda, Spin exchange in excitons, the quasicubic model and deformation potentials in II-VI compounds, *Phys. Rev. B* **2**, 4005 (1970).
- [34] K. Hestroffer, R. Mata, D. Camacho, C. Leclere, G. Tourbot, Y. M. Niquet, A. Cros, C. Bougerol, H. Renevier, and B. Daudin, The structural properties of GaN/AlN core-shell nanocolumn heterostructures, *Nanotechnology* **21**, 415702 (2010).
- [35] F. Glas, Critical dimensions for the plastic relaxation of strained axial heterostructures in free-standing nanowires, *Phys. Rev. B* **74**, 121302 (2006).
- [36] S. Raychaudhuri and E. T. Yu, Critical dimensions in coherently strained coaxial nanowire heterostructures, *J. Appl. Phys.* **99**, 114308 (2006).
- [37] L. Rigutti, I. Blum, D. Shinde, D. Hernández-Maldonado, W. Lefebvre, J. Houard, F. Vurpillot, A. Vella, M. Tchernycheva, C. Durand, J. Eymery, and B. Deconihout, Correlation of microphotoluminescence spectroscopy, scanning transmission electron microscopy, and atom probe tomography on a single nano-object containing an InGaN/GaN multi-quantum well system, *Nano Lett.* **14**, 107 (2014).
- [38] J. Wrzesinski and D. Fröhlich, Two-photon and three-photon spectroscopy of ZnO under uniaxial stress, *Phys. Rev. B* **56**, 13087 (1997).
- [39] J.-M. Chauveau, M. Teisseire, H. Kim-Chauveau, C. Morhain, C. Deparis, and B. Vinter, Anisotropic strain effects on the photoluminescence emission from heteroepitaxial and homoepitaxial nonpolar (Zn,Mg)O/ZnO quantum wells, *J. Appl. Phys.* **109**, 102420 (2011).
- [40] S.-H. Jang and S. F. Chichibu, Structural, elastic, and polarization parameters and band structures of wurtzite ZnO and MgO, *J. Appl. Phys.* **112**, 073503 (2012).
- [41] Nextnano - Software for Semiconductor Nanodevices, <http://www.nextnano.de/>.
- [42] F. Vurpillot and X. Sauvage, editors, in *Atom Probe Tomography* (Academic Press, Cambridge, MA, 2016), p. iii.
- [43] E. P. Silaeva, L. Arnoldi, M. L. Karahka, B. Deconihout, A. Menand, H. J. Kreuzer, and A. Vella, Do dielectric nanostructures turn metallic in high-electric Dc fields?, *Nano Lett.* **14**, 6066 (2014).
- [44] M. Lange, J. Kupper, C. P. Dietrich, M. Brandt, M. Stölzel, G. Benndorf, M. Lorenz, and M. Grundmann, Exciton localization and phonon sidebands in polar ZnO/MgZnO quantum wells, *Phys. Rev. B* **86**, 045318 (2012).
- [45] A. Ashrafi, Exciton localization in inhomogeneously broadened ZnO/Mg<sub>x</sub>Zn<sub>1-x</sub>O quantum wells, *J. Appl. Phys.* **107**, 123527 (2010).
- [46] H. Zhu, C. X. Shan, B. H. Li, Z. Z. Zhang, J. Y. Zhang, B. Yao, D. Z. Shen, and X. W. Fan, Enhanced photoluminescence caused by localized excitons observed in MgZnO alloy, *J. Appl. Phys.* **105**, 103508 (2009).
- [47] N. Rolland, D. J. Larson, B. P. Geiser, S. Duguay, F. Vurpillot, and D. Blavette, An analytical model accounting for tip shape evolution during atom probe analysis of heterogeneous materials, *Ultramicroscopy* **159**, 195 (2015).
- [48] S. Koelling, A. Li, A. Cavalli, S. Assali, D. Car, S. Gazibegovic, E. P. A. M. Bakkers, and P. M. Koenraad, Atom-by-atom analysis of semiconductor nanowires with parts per million sensitivity, *Nano Lett.* **17**, 599 (2017).